Advances in Water Resources 163 (2022) 104167

Contents lists available at ScienceDirect

Advances in Water Resources

journal homepage: www.elsevier.com/locate/advwatres

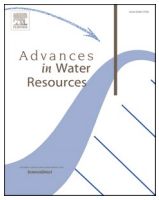

Pore-scale dynamics for underground porous media hydrogen storage

Maksim Lysyy *, Geir Ersland, Martin Fernø

Department of Physics and Technology, University of Bergen, Allégaten 55, 5007 Bergen, Norway

ARTICLE INFO

Keywords:
Underground hydrogen storage
Microfluidics
Residual trapping
Dissolution rates
Contact angle hysteresis

ABSTRACT

Underground hydrogen storage (UHS) has been launched as a catalyst to the low-carbon energy transitions. The limited understanding of the subsurface processes is a major obstacle for rapid and widespread UHS implementation. We use microfluidics to experimentally describe pore-scale multiphase hydrogen flow in an aquifer storage scenario. In a series of drainage-imbibition experiments we report the effect of capillary number on hydrogen saturations, displacement/trapping mechanisms, dissolution kinetics and contact angle hysteresis. We find that the hydrogen saturation after injection (drainage) increases with increasing capillary number. During hydrogen withdrawal (imbibition) two distinct mechanisms control the displacement and residual trapping – I1 and I2 imbibition mechanisms, respectively. Local hydrogen dissolution kinetics show dependency on injection rate and hydrogen cluster size. Dissolved global hydrogen concentration corresponds up to 28% of reported hydrogen solubility, indicating pore-scale non-equilibrium dissolution. Contact angles show hysteresis and vary between 17 and 56° Our results provide key UHS experimental data to improve understanding of hydrogen multiphase flow behaviour.

1. Introduction

As a no-carbon energy carrier, hydrogen may play a significant role in the energy transition needed to reach net-zero societies. Hydrogen implementation in transport, heating and power generation will require large-scale seasonal storage, and underground hydrogen storage (UHS) in aquifers has been proposed as one option (Carden and Paterson 1979; Lord et al., 2014). Technical aspects of UHS are similar to natural gas storge (UGS), where gas is injected in the subsurface (cushion gas) and is then withdrawn at peak demand (working gas). Although knowledge transfer from UGS is possible, high hydrogen mobility and its potential biogeochemical activity (Panfilov 2010) calls for caution and revision of conventional storage practices. Experience with commercial underground storage of pure hydrogen is limited to salt caverns (Ozarslan 2012). Underground aquifers have been used for town gas storage only, with hydrogen content up to 50–60% (Smigan et al., 1990; Panfilov 2016).

Hydrogen injection and withdrawal in underground porous formations involve complex displacement and trapping mechanisms, controlled by hydrogen flow properties and interactions with reservoir fluids and rocks. The understanding of hydrogen flow physics and trapping in porous media is therefore essential to establishing reliable storage models for lab-scale tests, feasibility studies and piloting. Most porous media research on hydrogen is mainly focused on biogeochemical interactions (Berta et al., 2018; Flesch et al., 2018; Bo et al., 2021), but there are fewer fundamental studies reporting multiphase flow data with the dominance of the numerical modelling approaches (Lubon and Tarkowski 2021; Lysyy et al., 2021; Mahdi Kanaani 2022). Most numerical studies use extrapolated flow functions not specifically measured for hydrogen; thus experimental efforts are needed to improve the hydrogen flow modelling. A single reported experimental core-scale study found that hydrogen-water relative permeability is independent of pressure and temperature conditions (Yekta et al., 2018). A major concern is that the displacement is prone to front instabilities and viscous fingering due to an unfavourable hydrogen-water mobility ratio. Microscopic viscous fingers were confirmed with laboratory models (Paterson 1983). In addition, hydrogen withdrawal will be associated with loss caused by residual and dissolution trapping. Unlike CO_2 sequestration, residual and dissolution trapping are not desirable in UHS as it leads to unrecoverable hydrogen, thus representing a permanent loss (Carden and Paterson 1979). UHS involves many injection-withdrawal cycles, and the residually trapped hydrogen may reconnect during subsequent hydrogen injections, known as hysteresis.

Microfluidic experiments are perfectly suited for visualization of porous media hydrogen flow, thereby providing direct evidence of the proposed displacement and trapping mechanisms to corroborate core-

* Corresponding author.
E-mail address: maksim.lysyy@uib.no (M. Lysyy).

https://doi.org/10.1016/j.advwatres.2022.104167
Received 20 December 2021; Received in revised form 7 March 2022; Accepted 9 March 2022
Available online 11 March 2022

scale measurements. Due to the 2D nature of the micromodels and their limited volume, microfluidic experiments should mainly focus on the qualitative rather than quantitative results. Extrapolation of quantitative 2D data to 3D natural environment should be done with caution, best achieved through pore-scale modelling. In particular hydrogen contact angle measurements assist the pore-scale models in estimating upscaled relative permeability and capillary pressure functions, which can be used as input for numerical studies at field scale (Hashemi et al., 2021).

Classical pore-scale displacement theory defines four displacement mechanisms which may result in residual trapping – piston-like, snap-off, I1 imbibition, and I2 imbibition (Lenormand et al., 1983). Dissolution trapping occurs when the residually trapped phase dissolves in water, controlled by the trapped phase diffusivity and solubility. Hydrogen solubility studies relevant for UHS demonstrated inconsistencies due to missing experimental support and/or different measurement approaches (De Lucia, Pilz et al. 2015; Li et al., 2018; Lopez-Lazaro et al., 2019; Chabab et al., 2020).

Contact angle measurements are commonly used in multiphase transport research to understand the effects of wettability and capillary pressure and relative permeability hysteresis on fluid systems. The hydrogen-water system is still not adequately investigated and lack consistent and systematic approaches. However, hydrogen contact angles have been derived for basalt (Al-Yaseri and Jha 2021) and measured for quartz (Iglauer et al., 2021) and sandstone (Hashemi et al., 2021) rocks, and the results showed discrepancies in terms of pressure, temperature and salinity effects.

Overall, pore-scale displacement and trapping mechanisms are well described for CO_2 sequestration (Buchgraber et al., 2012; Cao et al., 2016; Chang et al., 2016; Hu et al., 2017; Chang et al., 2020) but remains, to our knowledge, unaddressed for hydrogen. Our work examines hydrogen flow behaviour in an initially water-filled micromodel relevant for UHS in aquifers. We perform a series of injection (drainage) and withdrawal (imbibition) experiments to qualitatively describe pore-scale hydrogen displacement and trapping mechanisms. With image analysis, we quantify hydrogen dissolution kinetics and measure contact angles. This study is relevant for readers seeking to understanding of hydrogen flow physics in porous media and adds new data to experimental dataset.

2. Materials and methods

2.1. Micromodel

All drainage and imbibition experiments were conducted in a silicon-wafer micromodel based on natural sandstone pore patterns with a large variation in grain and pore sizes and shapes. Extracted from the scanning electron microscope image of a representative sandstone thin section and slightly modified to enable flow, the 2D pore network was etched into silicon wafer with deep reactive ion etching, DRIE (Hornbrook et al., 1991; Buchgraber et al., 2012). The DRIE realistically reproduces topological features such as high pore body to pore throat ratio, coordination number (4–8), sharp pore walls and surface roughness (100 nm). The exact reproduction of pore and pore throat sizes generate capillary forces at the magnitude relevant for real porous rocks. The heterogeneous mineralogy is, however, not reproduced, i.e. no clay and/or calcite minerals present. The silicon dioxide layer on the micromodel surfaces prevents hydrogen adsorption. Four ports, etched through the micromodel bottom, facilitate external access to the porous network, whereas two high-permeable fracture channels between the ports allow to easily distribute the injected fluids. The micromodel bottom (silicon wafer) and top (borosilicate glass) surfaces were connected through anodic bonding, resulting in the hydrophilic pore network. The micromodel hydrophilic nature allowed us to distinguish between the injected fluids. Under microscopic view (Fig. 2), hydrogen (light blue) develops a convex curvature towards water (blue) and the grains.

The etched porous network has the length x width x depth dimensions of 2.8 cm x 2.2 cm x 0.0030 cm respectively and porosity of ~60%, yielding the pore volume of ~11 μL. The average pore diameter is in the order of 100 μm, with the grain size and pore throat length distributions of 100–7900 μm^2 and 10–200 μm, respectively (Alcorn et al., 2020). The pore network extraction tends to increase the total micromodel porosity compared with the representative rock, and the micromodel porosities up to 46–55% can be found in the literature (Buchgraber et al., 2012; Chang et al., 2019; Wu et al., 2021). Our pore network was based on the thin rock section, containing both small and large pore clusters. The pore network was repeated 36 (4 × 9) times and stitched together on the micromodel surface, resulting in relatively high total porosity of ~60%. Note, however, that our microscope provided the observations of the micromodel field of view (FoV) only, which is approximately 1% of the whole micromodel area. The local FoV porosity is in the order of ~30%, which is closer to the natural rocks.

2.2. Experimental set-up and procedure

The micromodel was mounted in the PEEK holder and connected to two Quizix pumps through 1/16'' PEEK and stainless-steel tubing (Fig. 1a). Quizix SP-5200 pump (cylinder C5000–10K-SS-AT) was filled with pure hydrogen (≥99.999%), whereas Quizix QX pump contained distilled water. The micromodel was illuminated by a light source (Photonic LED F1 Cold light 5500 K). A microscope (Nikon SMZ1500), connected to a camera (Nikon D7100) and computer, provided direct real-time observations of the FoV. Experimental data was acquired through live-view video recordings, with the frame rate 29.97 fps and the resolution of 0.5 pixels/μm.

Prior to every run, consisting of hydrogen and water injections, the pore-space was initially 100% saturated with distilled water. Every experiment consisted of one hydrogen injection (drainage) and one water injection (imbibition) from two opposite inlets, creating a diagonal flow through the pore network. All injections used a pore-pressure of $p = 5$ bar and room temperature. Constant pressure was maintained with a hydrogen-filled pump, whereas a water-filled pump performed water withdrawal/injection at constant flow rates. Hydrogen injections (drainage) were initiated by water withdrawal and lasted until between 50 and 500 water pore volumes (PV) were withdrawn after hydrogen invasion, enabling quasi steady-state. Subsequently, water injection (imbibition) started with the same flow rate and the injection was maintained until hydrogen was completely dissolved, thereby running a single cycle of hydrogen injection-withdrawal only. The micromodel was then cleaned with distilled water to remove any residual hydrogen and to re-saturate the pore space with 100% distilled water, making the system ready for the next experiment. Four different flow rates were applied: 0.1, 1, 10, and 50 mL/h, with corresponding capillary numbers (N_{Ca}) calculated from the equation: $N_{Ca} = U \bullet \mu / \sigma$, where U is flow velocity [m/s], μ is the wetting-phase (water) viscosity [Pa•s], and σ is the interfacial tension [N/m]. Flow velocity, U, was calculated as $U = Q/(L \bullet d \bullet \phi)$, with Q = rate [m^3/s], L = near-inlet length inside the micromodel [m], d = porous network depth [m], ϕ = porosity [fraction]. Hydrogen interfacial tension, σ, at experimental pressure was calculated to 0.072 N/m based on the empirical formulation (Massoudi and King 1974). The calculated capillary numbers allowed to locate our experiments on the log(N_{Ca})-log(M) stability diagram (Fig. 1b), where M is defined as the hydrogen-water viscosity ratio.

2.3. Relevance of experimental conditions

Our experiments were run under low pressure and with distilled water. The reservoir brine salinity may affect the gas surface properties: the gas-brine interfacial tension (Duchateau and Broseta 2012) and contact angles (Jafari and Jung 2019) increase with increasing salinity. These correlations are yet to be confirmed for hydrogen-brine systems

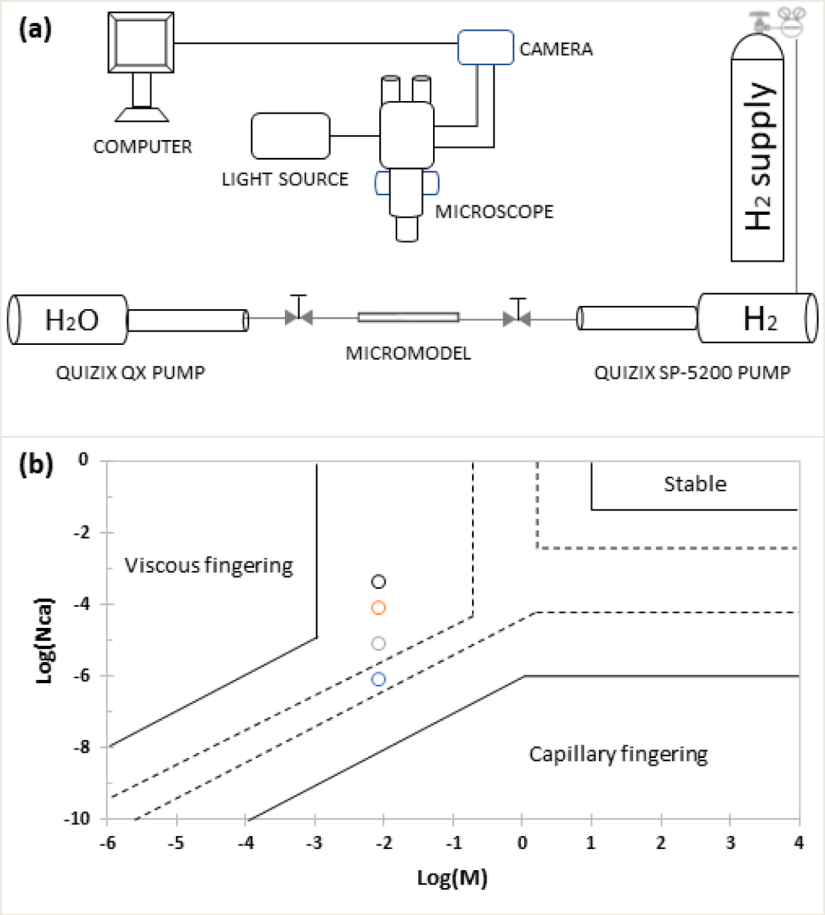

Fig. 1. *(a)* Schematic of experimental set-up with the micromodel, pumps for pressure control and fluid injection/withdrawal, the microscope, and the camera for live-view video recordings of the porous network. Hydrogen and water are injected from two opposite inlets. *(b)* Log(N_{Ca})-Log(M) stability diagram, where the solid lines represent the originally proposed boundaries (Lenormand et al., 1988), and the dashed lines denote the extended boundaries (Zhang et al., 2011). The circles locate experiments performed in this work. Reynold number (*Re*) ranges between 0.006 and 3.1, where $Re=\rho \cdot U \cdot D_{50}/\mu$ with ρ=water density [kg/m^3] and D_{50}=median grain diameter [$=1.1 \cdot 10^{-4}$ m].

and should be addressed in future studies. Low pressure was selected in our work due to the safety risks associated with hydrogen flammability and equipment compatibility under high pressure. Hydrogen properties affecting 2D porous media multiphase flow (viscosity and H_2—H_2O interfacial tension) do not vary significantly with increasing storage depths (increasing pressure and temperature), unlike many other gases like CO_2, N_2 and CH_2 (Beckingham and Winningham 2020; al. 2022). Pressure-dependant variations in hydrogen density play an important role in gravity-dominated 3D problems and thus are assumed to be insignificant in our 2D microfluidic study. Moreover, one of the hydrogen storage projects was operated at pressures down to 5–10 bars in the Argentinian depleted gas field (Pérez et al., 2016). Our low-pressure study is therefore relevant for the real storage conditions.

2.4. Image analysis

Experimental data was quantified with image analysis in the open-source ImageJ software. Hydrogen saturations were estimated based on colour thresholding, permitting to calculate local FoV porosity and distinguish hydrogen from water. Dissolution data was obtained by measuring the areal decrease of the hydrogen phase with time. Contact angles were measured using an angle tool. Static contact angles were measured when the hydrogen-water interface did not move, whereas paused videos allowed to measure dynamic contact angles when the hydrogen-water interface moved during water withdrawal/injection. Receding contact angles were measured when hydrogen displaced water (drainage). Advancing contact angles were measured when water displaced hydrogen (imbibition). Note that the image analysis is dependant on the image resolution, segmentation, and user adjustments. The image resolution was high enough to distinguish between hydrogen and water. In some cases, the light source limitations resulting in the image gradients required pre-processing of the images, with the manual segmentation of fluids.

3. Results and discussion

3.1. Hydrogen saturation establishment during drainage

Hydrogen invaded the pores immediately after entering the FoV, indicating that non-wetting phase invasion occurred on millisecond scale independent of capillary number (N_{Ca}). This is consistent with previous micromodel studies in oil/air-water systems (Mohanty et al., 1987; Moebius and Or 2012; Armstrong and Berg 2013). Rapid hydrogen pore invasion serves as indirect evidence of hydrogen non-wetting nature (Andrew et al., 2015), which was directly confirmed by contact angle measurements (detailed in Section 3.4).

3.1.1. Initial hydrogen saturation

The FoV hydrogen saturation (Sg) after drainage increased with increasing N_{Ca} (Fig. 2), as expected from classical pore-scale displacement theory (Lenormand et al., 1983). Hydrogen invasion into neighbouring pore clusters was restricted by narrow pore throats with higher capillary entry pressures. Pores invaded by hydrogen were predominantly saturated with hydrogen, with some visible water accumulations (droplet forms) on the pore bottom due to surface roughness (white arrows in Fig. 2). Number of water droplets were largest at upper medium and high N_{Ca}, whereas they were absent at low N_{Ca} at the end of drainage. At the hydrogen breakthrough, however, water droplets formed even at low N_{Ca} (Fig. 3). With continued hydrogen injection the droplets were displaced, likely due to (1) the hydrophilic micromodel

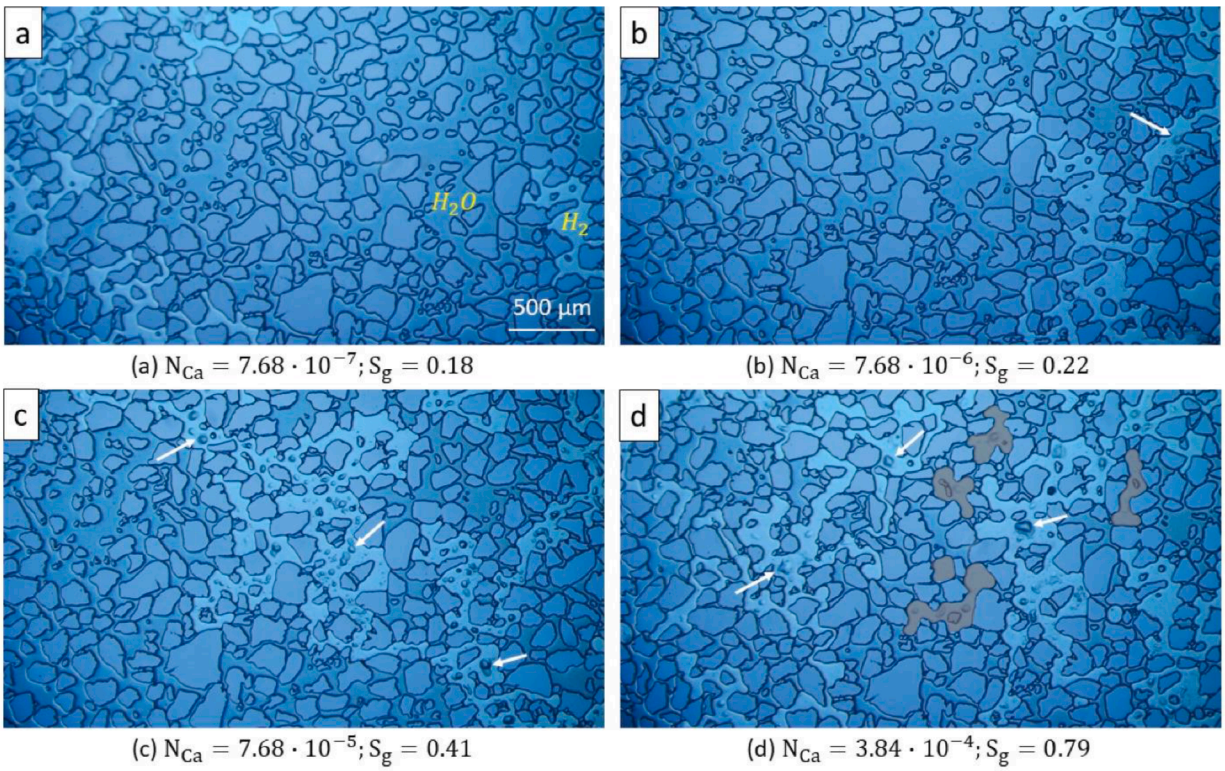

Fig. 2. FoV hydrogen (light blue) saturation (Sg) after drainage at various capillary numbers (N_{Ca}); the remaining pores were saturated with water (blue). Hydrogen was injected from the top right in every image. Sg increased with increasing N_{Ca}: *(a)* Sg=0.18 at NCa=$7.68 \cdot 10^{-7}$, *(b)* Sg=0.22 at N_{Ca}=$7.68 \cdot 10^{-6}$, *(c)* Sg=0.41 at N_{Ca} =$7.68 \cdot 10^{-5}$, *(d)* Sg=0.79 at N_{Ca} =$3.84 \cdot 10^{-4}$. The white arrows indicate water droplet accumulations in the surface roughness in the micromodel bottom. The hydrogen phase remained connected from low (image a) to upper medium (image c) N_{Ca}. At high N_{Ca} (image d) parts of the hydrogen phase became disconnected (indicated in grey). The drainage capillary desaturation curve was calculated based on Sg and N_{Ca} values and found in supplementary materials (Fig. S1).

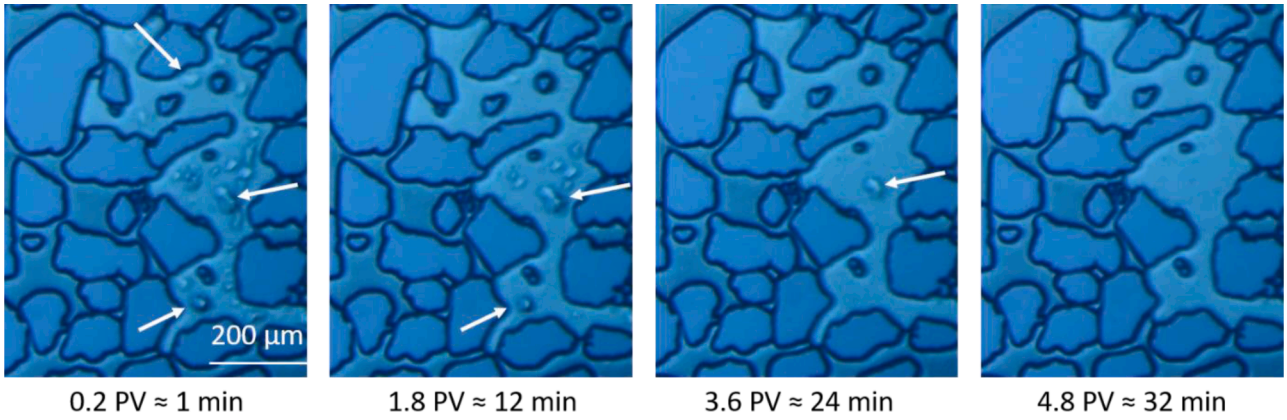

Fig. 3. Water droplets (white arrows) displacement by hydrogen during drainage at $N_{Ca} = 7.68 \cdot 10^{-7}$. Water droplets residing below hydrogen in the surface roughness of the micromodel were gradually displaced by hydrogen. Hydrogen percolation was restricted by small pore throats.

surfaces with high water phase connectivity through connected wetting films, and/or (2) water evaporation in hydrogen. The water droplet displacement/evaporation demonstrated the pore-scale efficiency of low-N_{Ca} drainage when multiple pore-occupancies establish in hydrophilic systems. From this we could expect that hydrogen injection strategies that result in pore-occupancy by hydrogen phase only (no pore water) will decrease water-cut upon hydrogen withdrawal in aquifer storage, improving overall storage performance. Low-N_{Ca} hydrogen injection may therefore be preferred from the perspective of the pore-occupancies.

3.1.2. *Hydrogen connectivity*

The non-wetting phase connectivity defines if the phase is connected through the pore clusters. The hydrogen connectivity was high at low and medium N_{Ca}, with observations of several connected gas paths (Fig. 2a-c). At high N_{Ca}, both connected and disconnected hydrogen phases established (Fig. 2d), with disconnected hydrogen phase accounting for ~ 11% of the total FoV hydrogen saturation. The predominant mechanism for disconnected hydrogen was Roof snap-off (Roof 1970) due to the front interface destabilization after entering the neighbouring pore. To maintain capillary equilibrium, water thickens in the pore throat, leading to the non-wetting phase (hydrogen in our case) disconnection. For Roof snap-off to occur, high water availability is

required near the pore throat and the non-wetting phase must pass the pore throat for a distance of at least seven times the throat radius. Snap-off controlled by capillary pressure is expected in smaller pore throats. In our work, Roof snap-off occurred in small (15 μm) and large (25 μm) pore throats, without occurring in neighbouring pore throats of similar sizes (Fig. 4). This implies that Roof snap-off was a local phenomenon, likely controlled by water mobility and availability, as suggested for drainage snap-off in a CO_2-brine system (Andrew et al., 2015). The pore throat water thickening, which was believed to cause hydrogen snap-off, was not possible to confirm visually because of sub-second snap-off and insufficient microscope resolution to detect thin wetting films. Before snap-off occurred in small and large pores (Fig. 4), the distance propagated by hydrogen corresponded to ~ 35 and 15 times of the pore throat radius respectively, fulfilling the condition for Roof snap-off.

Snap-off during drainage is less common than in imbibition and is still not appropriately investigated. In the seminal work of Roof (1970), the criteria for drainage snap-off were linked to local conditions – water availability, pore throat and interface size, wettability. The drainage snap-off dependency on global dynamic conditions – viscosity ratio, compressibility, capillary number – were proposed (Deng et al., 2015; Herring et al., 2018). Our results suggest that drainage snap-off was triggered by both local and global factors. The snap-off independence on pore throat sizes (Fig. 4) showed local features of snap-off events, whereas the snap-off occurrence at high N_{Ca} only suggests that snap-off drainage was correlated to global dynamic parameter – N_{Ca}.

Snap-off during and after drainage is undesired in seasonal hydrogen storage as this may lead to permanent hydrogen entrapment. In our work, most of disconnected hydrogen bubbles (Fig. 2d) did not reconnect during imbibition, resulting in a complete hydrogen dissolution. Although the highest hydrogen saturation (Fig. 2) was achieved at high N_{Ca} ($3.84 \cdot 10^{-4}$), high injection rates will not necessarily yield the maximum injection efficiency in aquifer storage projects considering the possibility for snap-off.

3.1.3. Flow regime

According to the logN_{Ca}-log$M$ phase diagram (Fig. 1b), unstable viscous-dominated displacement was expected to prevail over capillary-dominated flow. The logN_{Ca}-log$M$ phase diagram boundaries are, however, system-dependant (Zhang et al., 2011), and are not necessarily applicable for our micromodel. Neither viscous nor capillary fingering were possible to observe due to the limited FoV. Nevertheless, some indirect evidence of viscous and capillary flow regimes was observed locally. The establishment of the connected hydrogen phase, stopped by narrow pore throats, may show the importance of capillary fingering at low/medium N_{Ca}. Roof snap-off, caused by hydrogen penetration through narrow pore throats, indicate the dominance of viscous forces at high N_{Ca} (Zhang et al., 2011). Micromodel studies enabling to observe the entire micromodel at a wider N_{Ca} range will be beneficial for a direct determination of the dominating flow regime in hydrogen-water systems.

3.2. Displacement and residual trapping during imbibition

Hydrogen displacement and disconnection (residual trapping) was observed during imbibition, that started with water injection into the same fluid system which established after drainage. Imbibition proceeded in three main steps, common for all N_{Ca}: 1) displacement, 2) disconnection, 3) dissolution. An additional step (between steps 1 and 2) was observed at upper medium and high N_{Ca} – hydrogen redistribution caused by fluid displacement from outside the FoV. This section describes the first two steps, displacement and disconnection, in addition to redistribution. Dissolution will be described in Section 3.3.

3.2.1. Displacement mechanisms

Hydrogen displacement was mainly governed by I1 imbibition mechanism (Fig. 5a). Initially occupying three pores, hydrogen was forced into a single pore because of the curvature instability, resulting from the curvature detachment from the pore walls. Two other displacement mechanisms were common at specific N_{Ca}: piston-like displacement and redistribution. Piston-like displacement was observed at low N_{Ca}, where a stable displacement front moved through a single pore channel (Fig. 5b). The pore channel was surrounded by narrow pore throats, forcing water to displace hydrogen from one direction only. At upper medium and high N_{Ca}, hydrogen redistribution occurred (Fig. 5c), where the original hydrogen phase was first displaced and trapped, followed by a partial reconnection with surrounding hydrogen. This mechanism occurred because of high hydrogen saturation after upper medium/high-N_{Ca} drainage, permitting hydrogen movement through the entire micromodel during imbibition. Note that most of the hydrogen bubbles, disconnected due to Roof snap-off during drainage, remained disconnected during redistribution. Only a single hydrogen bubble in the FoV reconnected with the continuous hydrogen phase. The inability to reconnect resulted in a complete hydrogen bubble dissolution, demonstrating the disadvantages of the drainage snap-off.

3.2.2. Residual trapping

Hydrogen disconnection, leading to residual trapping, occurred mainly by I2 imbibition mechanism (Fig. 6a). Displacement from the

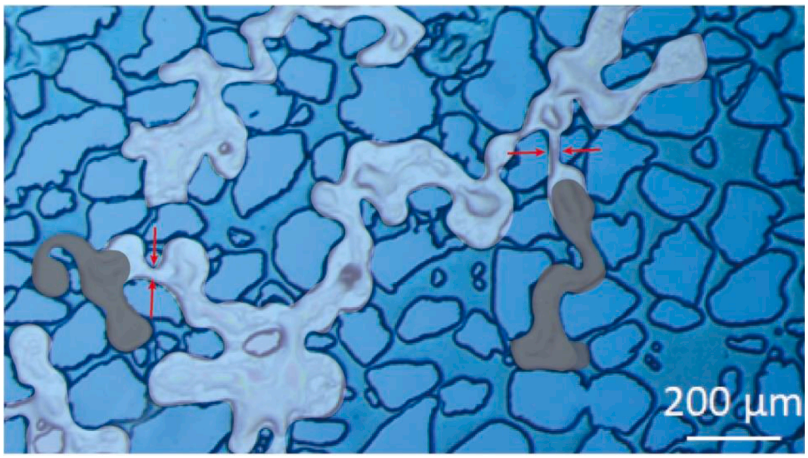

Fig. 4. Roof snap-off during drainage was observed at high N_{Ca}=$3.84 \cdot 10^{-4}$ only. Hydrogen phase distribution after breakthrough (white) changed within less than one second due to snap-off. The red arrows locate the pore throats where snap-off occurred, resulting in disconnected hydrogen bubbles (grey).

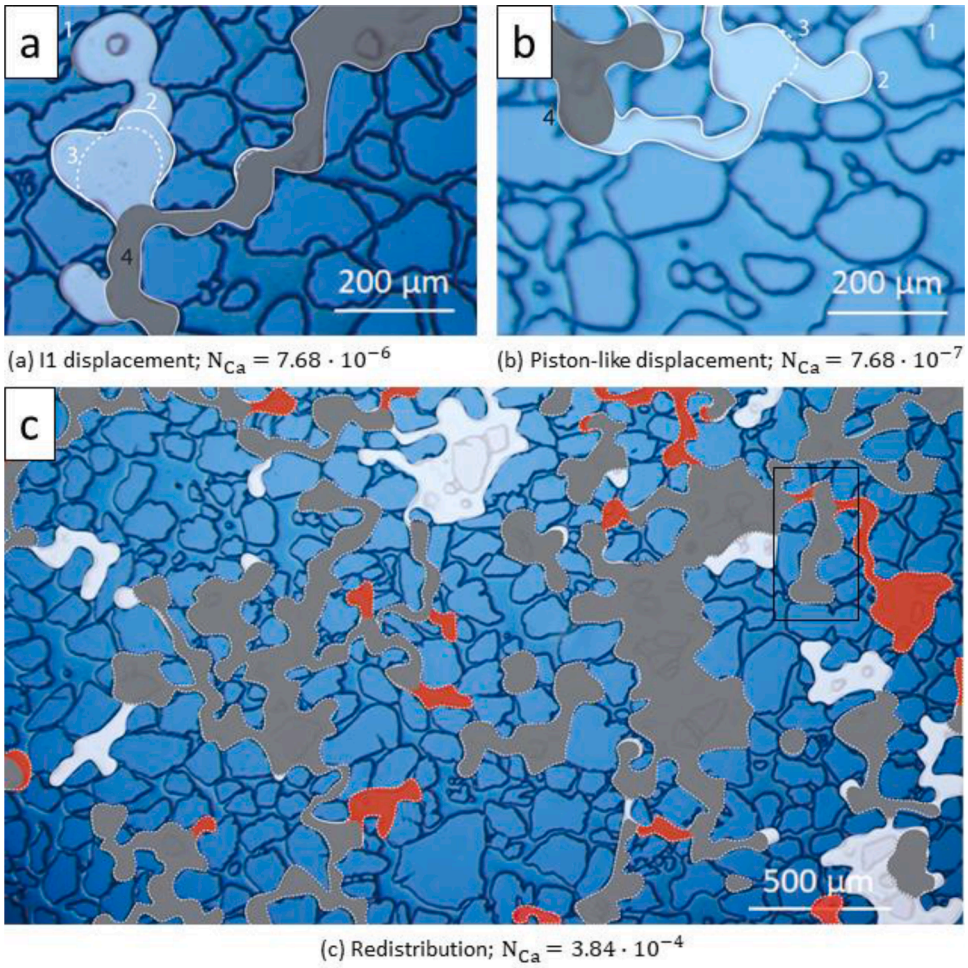

Fig. 5. Hydrogen displacement mechanisms during imbibition, where colors and outlines indicate the hydrogen phase after each time step t_i. *(a)* An example of the I1 type imbibition where hydrogen residing in several pores (t_1; white) was displaced ($t_{2,3}$; solid and dashed outlines) into a single pore (t_4; grey, $\Delta t_{4-1} = 1$ s). *(b)*Piston-like displacement was observed for low N_{Ca}=7.68•10^{-7}, where initial hydrogen phase (t_1; white) was displaced ($t_{2,3}$; solid and dashed outlines) with a stable front through a single pore channel (t_4; grey, $\Delta t_{4-1} = 9$ s). *(c)*Hydrogen redistribution was observed at higher $N_{Ca} \geq 7.68 \cdot 10^{-5}$. The original hydrogen phase distribution (t_1: white + grey) was first displaced by water and then reconnected with hydrogen phase (t_2: grey + red, $\Delta t_{2-1} = 20$ s) flowing from outside the FoV. Only a single disconnected hydrogen bubble reconnected with hydrogen phase during redistribution (black square), and most of the hydrogen bubbles remained disconnected. The raw image sequence of Fig. 5 is shown in the supplementary materials (Fig. S3) together with live-time FOV videos.

pore centre towards the pore wall resulted in hydrogen disconnection when the hydrogen-water interface reached the pore wall. The disconnected hydrogen occupied two pores. Trapping by bypass was observed at upper medium and high N_{Ca} (Fig. 6b). The water flow paths did not manage to invade the large hydrogen-saturated pore clusters with narrow pore throats, resulting in a significant hydrogen fraction being bypassed. The dominance of the I2 mechanism over bypass was likely due to topological reasons (high coordination number), permitting the transverse-to-hydrogen water flow paths. Bypass is expected in large pore clusters with narrow pore throats (Chatzis et al., 1983), consistent with our observations. However, at low and lower medium N_{Ca}, hydrogen did not occupy the large pore clusters (Fig. 2a,b), where bypass was observed at upper medium and high N_{Ca}. For a more general conclusion on the relative importance of I2 and bypass mechanisms, hydrogen must occupy the same pore clusters in all experiments, which is challenging to control in the heterogeneous pore space with the micromodels used in this study. Trapping by snap-off was not identified despite high micromodel aspect ratio and roughness, likely due to experimental conditions. Snap-off is expected to dominate at $N_{Ca} < 10^{-7}$ (Hu et al., 2017), whereas our experiments were conducted at $N_{Ca} \geq 7.68 \cdot 10^{-7}$. The FoV hydrogen saturation profiles were estimated for imbibition to construct the imbibition CDC and gas trapping curves (Fig. S2 and Fig. S1 in the supplementary materials, respectively).

3.3. Dissolution

3.3.1. Dissolution mechanisms

Dissolution of disconnected and trapped hydrogen was observed during prolonged water injection. Three dissolution mechanisms were identified (Fig. 7): one-end dissolution, two-end dissolution, and displacement dissolution. The one-end dissolution (Fig. 7a) was frequently observed at upper medium and high N_{Ca}, where hydrogen bubbles dissolved from one end only, reflecting the water flow direction. The rapidly developed waterfront, propagating through the micromodel in one main direction, was not able to enter narrow pore throats countercurrently against the main flow direction. Hence, dissolution initiated only from one end of the trapped hydrogen bubble, residing in the pore corners surrounded by narrow pore throats. The one-end dissolution was also observed in supercritical CO_2 dissolution in micromodel (Chang et al., 2016). The two-end dissolution mechanism (Fig. 7b) prevailed at lower medium N_{Ca} where the hydrogen bubbles were dissolved at both sides simultaneously. This mechanism was attributed to a more stable waterfront and greater water availability, originating from lower hydrogen saturation developed after drainage. The displacement dissolution mechanism (Fig. 7c) was characterized by mobilization of smaller hydrogen bubbles that were able to penetrate narrow pore throats. This mechanism was observed at upper medium and high N_{Ca} due to faster and more directed water flow. Overall, observed dissolution mechanisms suggest that hydrogen dissolution was governed by the waterfront velocity and direction, which in turn was controlled by N_{Ca}.

Two dissolution processes were detected independent of N_{Ca} – homogeneous and heterogeneous dissolution. They differed in terms of the microbubble final state at the end of dissolution. In homogenous dissolution, microbubbles dissolved completely, whereas the residual microbubbles accumulated at the surface roughness in heterogeneous dissolution. Homogenous/heterogeneous dissolution as well as

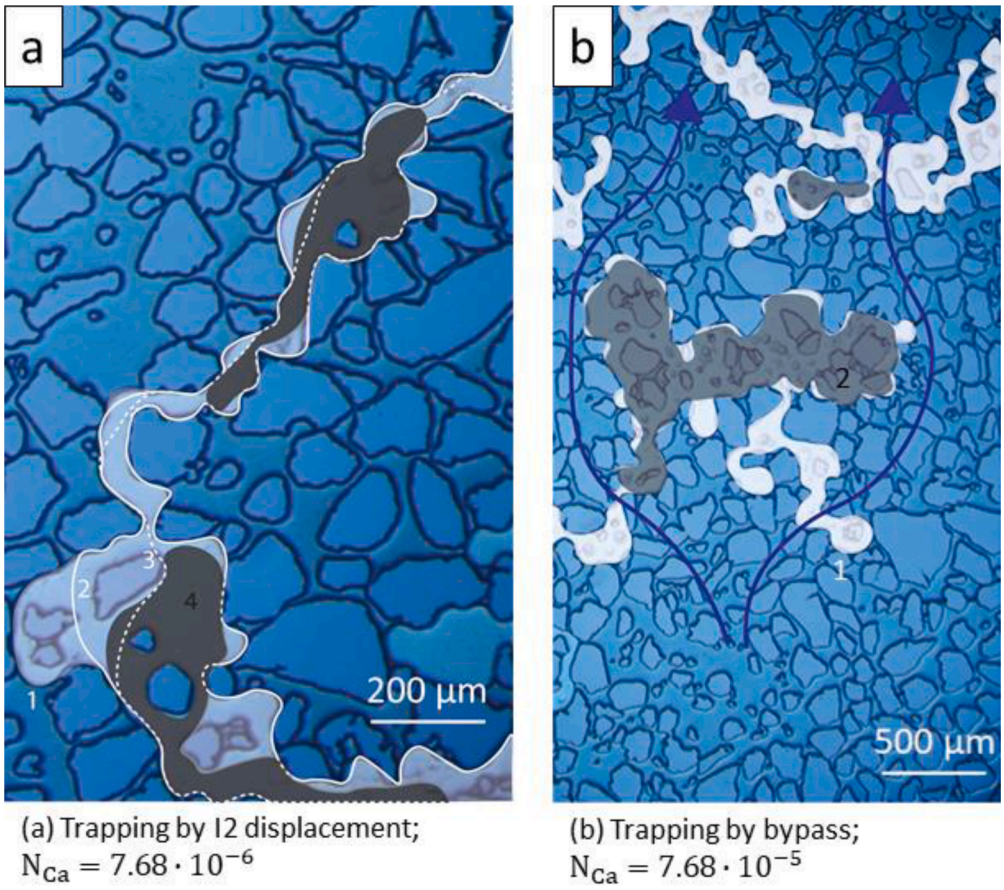

Fig. 6. Hydrogen trapping mechanisms during imbibition. Colors and outlines indicate the hydrogen phase after each time step t_i. *(a)* Trapping by I2 type imbibition resulting in residual trapping, where hydrogen originally residing in a single pore (t_1, white) was displaced towards the pore wall ($t_{2,3}$; solid and dashed outlines) until hydrogen disconnection occurred. The disconnected hydrogen occupied two pores (t_4; grey, $\Delta t_{4-1} = 1.3$ s). *(b)* Trapping by bypass was observed at $N_{Ca} \geq 7.68 \cdot 10^{-5}$. A hydrogen cluster residing in large pores surrounded by narrow pore throats (t_1, white) was bypassed by water (dark blue arrows; show the general water flow direction, but not the exact flow path through the pores) resulting in trapped hydrogen (t_2; grey, $\Delta t_{2-1} = 1$ s). The raw image sequence of Fig. 6 is shown in the supplementary materials (Fig. S4) together with live-time FOV videos.

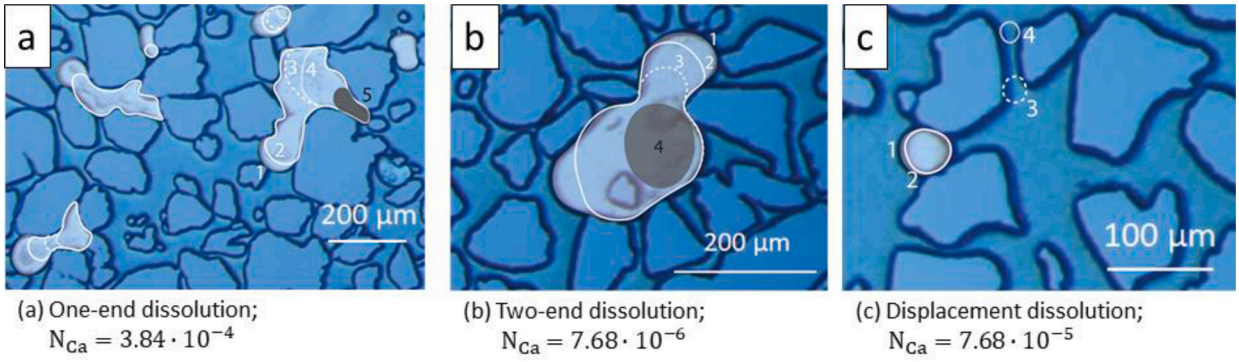

Fig. 7. Hydrogen dissolution mechanisms. Colors and outlines indicate the hydrogen phase after each time step t_i. *(a)* In one-end dissolution, the hydrogen bubbles (t_1, white) were dissolved from one end only ($t_{2,3,4}$; solid and dashed outlines) reflecting the water flow direction (left to right) until the hydrogen was partially (t_5, grey) or completely dissolved ($\Delta t_{5-1} = 22$ s). *(b)* In two-end dissolution, the hydrogen bubble (t_1, white) was dissolved from two ends ($t_{2,3}$; solid and dashed outlines) until partial dissolution (t_4, grey, $\Delta t_{4-1} = 134$ s). *(c)* In displacement dissolution, the hydrogen bubble (t_1, white) was displaced when its size decreased ($t_{2,3,4}$; solid and dashed outlines, $\Delta t_{4-1} = 5$ s) to below the pore throat gaps. One-end dissolution (a) and displacement dissolution (c) occurred at $N_{Ca} \geq 7.68 \cdot 10^{-5}$, whereas two-end dissolution (b) was common at $N_{Ca} = 7.68 \cdot 10^{-6}$. The one-end and two-end dissolution kinetics is quantified in Fig. 8. The raw image sequence of Fig. 7 is shown in the supplementary materials (Fig. S5) together with live-time FOV videos.

displacement dissolution (Fig. 7c) were also reported for CO_2 dissolution in micromodel (Buchgraber et al., 2012).

3.3.2. Dissolution kinetics

Local and global dissolution kinetics were estimated based on the image analysis. Local dissolution kinetics was quantified by calculating the temporal change in the individual hydrogen bubble size and the depletion rate (Fig. 8). As expected, time required for compete dissolution decreased with increasing N_{Ca} because of the faster water supply (Fig. 8a). The total dissolution time in every experiment was nearly equal and independent of the initial bubble area, implying simultaneous dissolution in the entire FoV. The depletion rate (Fig. 8b) was calculated as the depleted hydrogen mass per time interval between two sequential images: $Q_d = (\Delta A \cdot d \cdot \rho_{H2})/\Delta t$, where ΔA = decrease in individual hydrogen bubble area between two sequential images, d = porous network depth, ρ_{H2} = hydrogen density under experimental conditions ($4.12 \cdot 10^{-4}$ g/mL), Δt = time interval between two sequential images. The depletion rate changed with time, shifting from nearly constant values to increasing or decreasing trends. Similar discrepancies in depletion rate trends were also observed in pore-scale supercritical CO_2

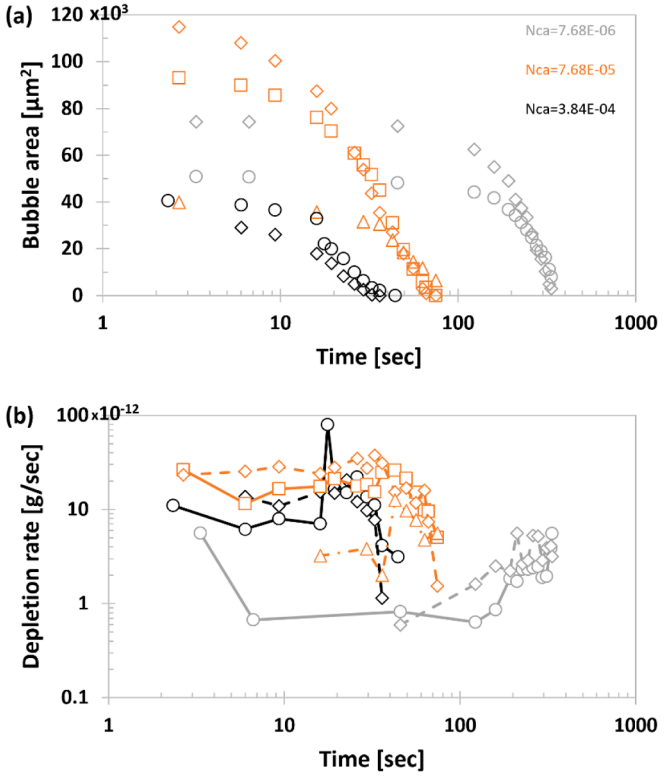

Fig. 8. Local dissolution kinetics. *(a)* Temporal change in bubble area for N_{Ca}; time required for complete dissolution decreased with increasing N_{Ca}. For the same N_{Ca}, the total dissolution time was equal, independent of initial bubble area size. *(b)* Depletion rate as a function of time was not constant. Average depletion rate was the fastest at N_{Ca}=7.68•10^{-5} and the slowest at N_{Ca}=7.68•10^{-6}. The depletion rate at N_{Ca}=7.68•10^{-4} was slower than at N_{Ca}=7.68•10^{-5} due to smaller initial bubble area. Black and grey circles show the dissolution kinetics of the hydrogen bubbles presented in Fig. 7a (marked with t_{1-5}) and in Fig. 7b, respectively.

dissolution, explained by the number of water flow paths, their direction (transverse or longitudinal), and the CO_2-water interface area (Chang et al., 2016). The average hydrogen depletion rate ranged from 2.3•10^{-12} to 22•10^{-12} g/*sec*, with the lowest rate observed at lower-medium N_{Ca} (expected) and the highest rate observed at upper medium N_{Ca} (unexpected). High N_{Ca} did not yield the highest depletion rate due to the smaller initial bubble size compared with upper medium-N_{Ca} cases. When comparing bubbles of similar size, high-N_{Ca} depletion rate was higher than upper medium-N_{Ca} (Table 2).

Global dissolution kinetics was analysed based on the FoV hydrogen saturation profiles during dissolution (Fig. 9). The global depletion rate (Fig. 9b) was calculated as follows: $Q_d\ (global) = (\Delta S_g \bullet V_p \bullet \rho_{H2})/\Delta t$, where ΔS_g = decrease in the FoV hydrogen saturation between two sequential images, V_p = micromodel pore volume, ρ_{H2} = hydrogen density under experimental conditions, Δt = time interval between two sequential images. The global depletion rate calculations assume that FoV hydrogen saturation profiles are representative for the entire micromodel. The global depletion rates showed non-constant trends, and on average varied between 3.6•10^{-10} to 277•10^{-10} g/*sec*, two orders of magnitude higher compared with local depletion rate of individual bubbles, similar to observations of CO_2 dissolution (Chang et al., 2016). The global depletion rate was the lowest at lower medium N_{Ca} and highest at high N_{Ca} (Table 2).

3.3.2.1. Dissolved hydrogen concentration and solubility. The averaged dissolved hydrogen concentration (Table 2) was calculated as the dissolved hydrogen amount per injected water mass between two

Table 1
Experimental conditions and micromodel properties.

Experimental conditions	Micromodel properties	Flow rate, Q [mL/h]	Flow velocity, U [m/s]	Capillary number, N_{Ca}	Capillary number classification
p = 5 bar t = 20 °C	L = 2.8 cm d = 30 µm	0.1 1	5.5•10^{-5} 5.5•10^{-4}	7.68•10^{-7} 7.68•10^{-6}	Low N_{Ca} Lower medium N_{Ca}
	V_p = 11 µL	10	5.5•10^{-3}	7.68•10^{-5}	Upper medium N_{Ca}
	ϕ=0.6	50	2.8•10^{-2}	3.84•10^{-4}	High N_{Ca}

Table 2
Hydrogen dissolution kinetics: average hydrogen depletion rate and dissolved hydrogen concentration in injected water mass.

Capillary number, N_{Ca}	Initial bubble area, A_i [µm^2]	Depletion rate, Q_d [g/*sec*]	Dissolved concentration, C [mol/kg]	Concentration relative to H_2 solubility, C/C_s [%]
7.68•10^{-6}	74•10^3	3.3•10^{-12}	5.9•10^{-6}	0.15
	52•10^3	2.3•10^{-12}	4.2•10^{-6}	0.10
	Global	3.6•10^{-10}	6.4•10^{-4}	16.0
7.68•10^{-5}	120•10^3	22•10^{-12}	3.9•10^{-6}	0.10
	99•10^3	17•10^{-12}	3.1•10^{-6}	0.08
	40•10^3	6.2•10^{-12}	1.1•10^{-6}	0.03
	Global	63•10^{-10}	11•10^{-4}	28.3
3.84•10^{-4}	43•10^3	16•10^{-12}	0.6•10^{-6}	0.01
	36•10^3	12•10^{-12}	0.4•10^{-6}	0.01
	Global	277•10^{-10}	9.9•10^{-4}	24.7

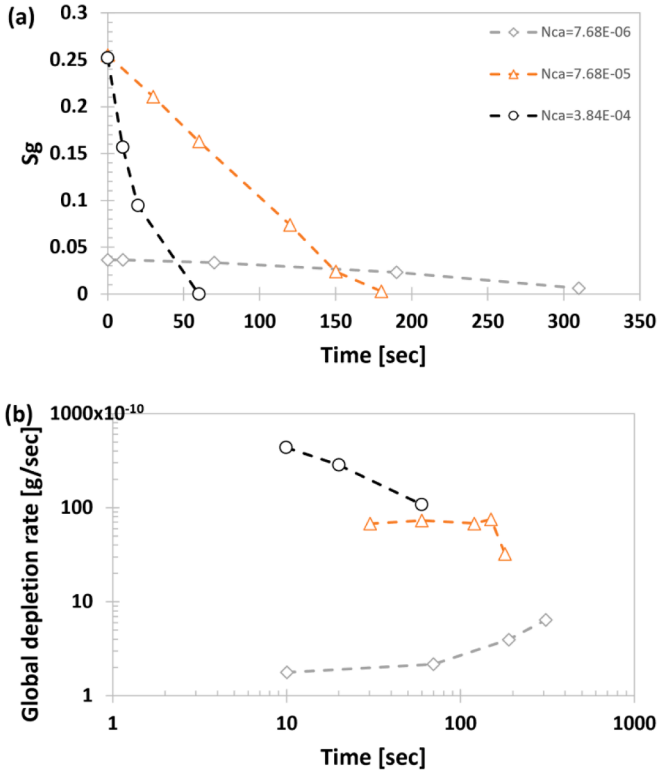

Fig. 9. Global dissolution kinetics. *(a)* Change in hydrogen saturation (Sg) as a function of time at various N_{Ca}. Sg was calculated in the FoV under the assumption to approximate the entire micromodel. *(b)* Global depletion rate as a function of time was not constant; being the fastest at N_{Ca}=3.84•10^{-4} and the slowest at N_{Ca}=7.68•10^{-6}. The global depletion rate was two orders of magnitude faster than the depletion rate of individual bubbles (Fig. 8).

sequential images according to the formula: $C = Q_d/(M_{H2} \cdot Q \cdot \rho_{H2O})$, where Q_d = hydrogen depletion rate, M_{H2} = hydrogen molar mass, Q = water injection rate, ρ_{H2O} = water density. These calculations were based on the mass balance principle, assuming that hydrogen depletion is solely controlled by dissolution and water advection (Chang et al., 2016; Chang et al., 2019). Hydrogen depletion will be controlled by diffusion when the water phase is immobile, which is not the case in our work where water is continuously injected during imbibition. In local dissolution, the dissolved individual hydrogen bubble concentration ranged between $0.4 \cdot 10^{-6}$ and $5.9 \cdot 10^{-6}$ mol/kg. In global dissolution, the dissolved hydrogen concentration varied from $6.4 \cdot 10^{-4}$ to $11 \cdot 10^{-4}$ mol/kg, corresponding to 16.0% and 28.3% of the hydrogen solubility under the applied experimental conditions (Chabab et al., 2020). Lower-than-solubility hydrogen concentrations indicate non-equilibrium hydrogen dissolution in our work, conflicting with classic equilibrium dissolution theories applied in numerical modelling (Pruess and Spycher 2007).

Non-equilibrium (slow) dissolution has also been reported for CO_2, both in experimental core- scale (Akbarabadi and Piri 2013; Chang et al., 2013) and pore-scale (Chang et al., 2016; Chang et al., 2019) studies, as well as numerical studies (Chen et al., 2018). For instance, CO_2 dissolution measurements in micromodels showed that the average CO_2 concentration varied between 0.25–13% of CO_2 solubility (Chang et al., 2016; Chang et al., 2019). They explained non-equilibrium dissolution by insufficient CO_2-water interface area and non-uniform CO_2-mobile water distribution. They argued that at reservoir-scale, where dissolution occurs at slower timescales, CO_2 dissolution after the injection stop will approach equilibrium unless strong heterogeneity is present. In hydrogen aquifer storage, hydrogen is cyclically injected and withdrawn at high rates, and we therefore speculate that non-equilibrium dissolution may play an important role.

3.4. Contact angles

3.4.1. Static and dynamic contact angles

Static (θ_S) and dynamic (θ_D) contact angles were measured during drainage and imbibition. Each measurement was performed five times at the same measuring point and then averaged, with the uncertainty represented as standard deviation. The measured contact angles (Fig. 10) varied from 17 to 56°, similar to contact angles of 22–45° for hydrogen-water-sandstone systems (Yekta et al., 2018; Hashemi et al., 2021). Our results confirmed that the micromodel is hydrophilic when exposed to hydrogen. No clear relationship between contact angles and pore diameter emerged, although the contact angle range appeared to narrow with increasing pore diameter (majority of measurements performed in pores with diameter between 50 and 125 μm).

Four contact angle types – receding (θ_R), advancing (θ_A), static in drainage ($\theta_{S,DR}$) and static in imbibition ($\theta_{S,IM}$), were averaged for each experiment (Table 3) and plotted as a function of N_{Ca} (Fig. 11a). The θ_A were significantly higher than the θ_R, consistent with classic theories (Johnson and Dettre 1964). As expected, $\theta_A > \theta_{S,IM}$, but θ_R and $\theta_{S,DR}$ were surprisingly similar, $\theta_R \approx \theta_{S,DR}$. The similarity between θ_R and $\theta_{S,DR}$ could be linked to the experimental procedure. After hydrogen breakthrough under drainage, hydrogen injection continued through the connected hydrogen phase, and the $\theta_{S,DR}$ were measured when the interface movement terminated visually. In this state, despite being motionless, the interfaces did not reach the equilibrium due to continuous hydrogen injection. The measured $\theta_{S,DR}$ approached more dynamic than static states, resulting in $\theta_R \approx \theta_{S,DR}$, and were thus believed to be underestimated and less reproducible. On the other hand, the water breakthrough under imbibition resulted in hydrogen residual trapping, with several hydrogen clusters being bypassed by water. In these regions, the interface was believed to be surrounded by immobile water, thus approaching equilibrium and yielding $\theta_A > \theta_{S,IM}$. The lower θ_S reproducibility was also reported for CO_2 contact angle measurements in micromodels using similar experimental methods (Jafari and Jung 2017). Note that θ_D are more important for hydrogen storge than less reproducible θ_S because θ_D represent dynamic hydrogen injection/withdrawal.

3.4.1.1. Equilibrium contact angles. The equilibrium contact angles (θ_E) were estimated based on the following equation (Tadmor 2004): $\theta_E = \cos^{-1}\left(\frac{R_A \cdot \cos\theta_A + R_R \cdot \cos\theta_R}{R_A + R_R}\right)$, where $R_A = \left(\frac{\sin^3\theta_A}{2 - 3\cos\theta_A + \cos^3\theta_A}\right)^{\frac{1}{3}}$ and $R_R =$

Table 3
Average contact angles measured during drainage/imbibition and calculated equilibrium angles.

Capillary number, N_{Ca}	Drainage		Imbibition		Calculated Equilibrium angle, θ_E [deg]
	Static angle, $\theta_{S,DR}$ [deg]	Receding angle, θ_R[deg]	Static angle, $\theta_{S,IM}$ [deg]	Advancing angle, θ_A[deg]	
$7.68 \cdot 10^{-7}$	22 ± 5	23 ± 4	37 ± 4	40 ± 6	32
$7.68 \cdot 10^{-6}$	21 ± 6	21 ± 6	24 ± 5	39 ± 9	30
$7.68 \cdot 10^{-5}$	22 ± 6	24 ± 6	30 ± 8	40 ± 6	32
$3.84 \cdot 10^{-4}$	25 ± 4	22 ± 4	35 ± 4	47 ± 7	35

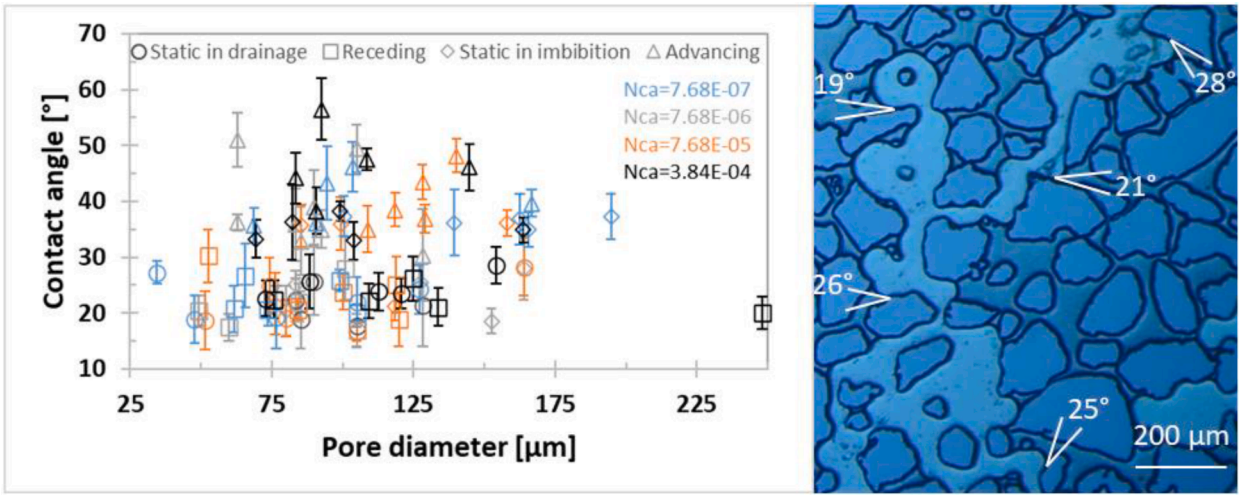

Fig. 10. Measured contact angles (left) and an example showing how static in imbibition angles were measured at N_{Ca}=$7.68 \cdot 10^{-6}$ (right).

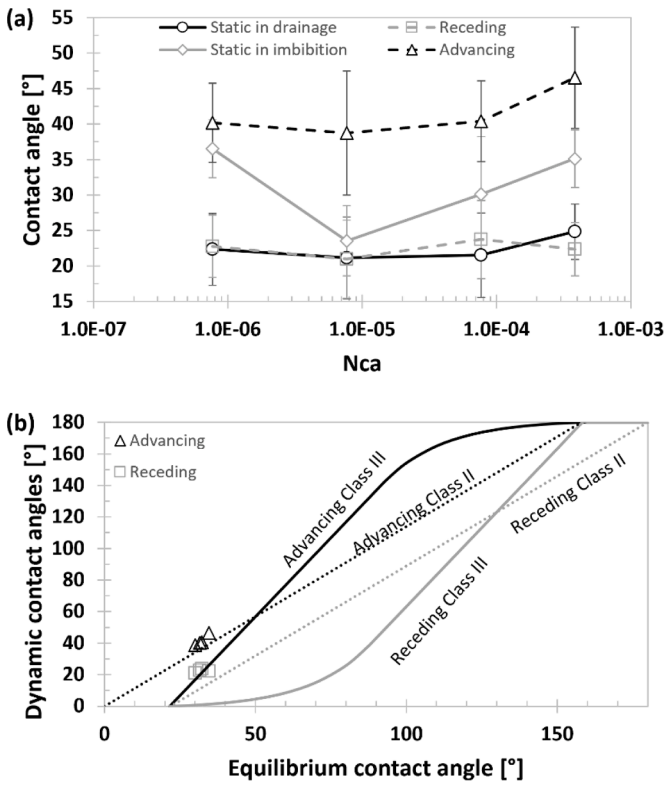

Fig. 11. *(a)* Average contact angles as a function of N_{Ca}. As expected, the advancing contact angles were higher compared with receding contact angles. *(b)* Dynamic (receding and advancing) contact angles as a function of calculated equilibrium angles. The solid and dashed curves represent the literature-based relationship (Morrow 1975) for Class III and Class II behaviour, respectively. Our results fit Class II behaviour.

$\left(\frac{\sin^3\theta_R}{2-3\cos\theta_R+\cos^3\theta_R}\right)^{\frac{1}{3}}$. The calculated θ_E were plotted together with the measured θ_A and θ_R (Fig. 11b), and compared with the original relationship based on the measurements through the capillary rise in polytetrafluoroethylene (PTFE) tubes (Morrow 1975). In the seminal work of Morrow, three different classes were defined, depending on the degree of surface roughness where the contact angles were measured: Class I – on smooth surfaces ($\theta_A = \theta_R$); Class II – on slightly roughened surfaces; and Class III – on well roughened surfaces. Our results showed that hydrogen-water fluid pair in a natural sandstone-based micromodel fit Class II behaviour, although the θ_R were slightly overestimated. This overestimation could be attributed to the difference in the measurement procedures. In our work, the θ_E were calculated based on the equation and the measured θ_A and θ_R in the heterogeneous micromodel with realistic pore geometries, whereas in Morrow (1975) both θ_E and θ_A/θ_R were experimentally measured in PTFE tubes which cannot account for the effect of the pore geometries.

The relationship between θ_E and θ_A/θ_R is essential for pore-scaling modelling, where Class III behaviour is widely implemented generally (Valvatne and Blunt 2004) and for hydrogen in particular (Hashemi et al., 2021). With known contact angles, relative permeability and capillary pressure functions can be predicted using pore-scale modelling and then upscaled for field-scale applications. Discrepancies between the pore-scale modelling approaches, which use Class III behaviour (well roughened surfaces), and our results showing Class II behaviour (slightly roughened surfaces) has a direct impact on understanding hydrogen pore-scale flow physics. Although the micromodel, used in this study, was reproduced with 100 nm surface roughness (Buchgraber et al., 2012), the micromodel may not be sufficiently rough to accurately reproduce the experimental results with pore-scale modelling. Mismatch between the experimental and simulated data may be expected when using Class III behaviour as the modelling input.

3.4.2. Contact angle hysteresis

Hysteresis was estimated for dynamic, $\Delta\theta_D = \theta_A - \theta_R$, and static contact angles, $\Delta\theta_S = \theta_{S,IM} - \theta_{S,DR}$ (Fig. 12a). As expected, static contact angle hysteresis ($\Delta\theta_S$) was lower than the dynamic one ($\Delta\theta_D$). No clear relationship was noted between $\Delta\theta_S$ and N_{Ca}, likely due to lower θ_S reproducibility in the micromodels as discussed earlier. On the other hand, $\Delta\theta_D$ seemed to depend on N_{Ca}, with nearly constant value until a slight increase at $N_{Ca} > 7.68\cdot10^{-5}$. The $\Delta\theta_D$ is expected to increase with increasing N_{Ca}, due to increasing θ_A and decreasing θ_R (Eral et al., 2013). A theoretical model for liquid-gas systems (Hoffman 1983) showed that the increase in θ_A becomes more pronounced at $N_{Ca} \geq 10^{-4}$–10^{-3}, comparable with our threshold $N_{Ca} > 7.68\cdot10^{-5}$. The $\Delta\theta_S$ is mainly attributed to surface roughness/heterogeneity (Joanny and Degennes 1984) or disjoining/conjoining pressure isotherm in the three-phase contact line (Kuchin and Starov 2016), whereas the $\Delta\theta_D$ is due to local surface blemishes which pin the three-phase contact line (Tadmor 2004). The $\Delta\theta_D$ dependency on N_{Ca} originates from competition between capillary and viscous forces (Friedman 1999).

Hysteresis may also be described by comparing the static and dynamic contact angles in each injection process, where drainage hysteresis describes the difference between $\theta_{S,DR}$ and θ_R and imbibition hysteresis refers to $\theta_{S,IM}$ and θ_A. Several models have been proposed to characterize imbibition hysteresis through the following equation (Jiang et al., 1979; Seebergh and Berg 1992; Li et al., 2013): $\frac{\cos\theta_{S,\ IM}-\cos\theta_A}{\cos\theta_{S,\ IM}+1} =$

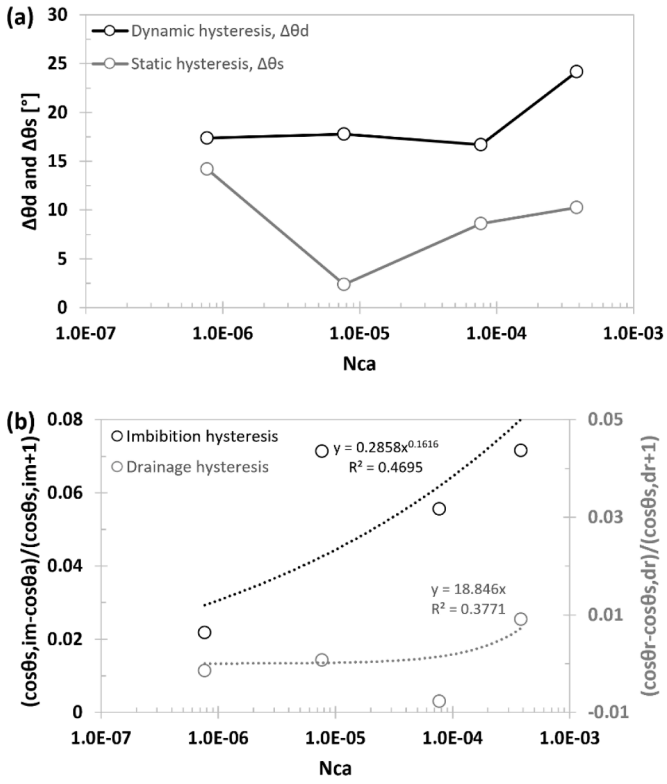

Fig. 12. Contact angle hysteresis. *(a)* Dynamic contact angle hysteresis, $\Delta\theta_D$, defined as the difference between advancing and receding contact angles, and static contact angle hysteresis, $\Delta\theta_S$, defined as the difference between static angles in imbibition and drainage. Dynamic contact angle hysteresis increased at $N_{Ca} > 7.68\cdot10^{-5}$, whereas no clear trend was observed for static angle hysteresis. *(b)* Drainage/imbibition contact angle hysteresis, which represent the difference between static and dynamic angles in each injection process. The data points were fitted with literature models (Jiang et al., 1979; Shi et al., 2018).

$B_1 \cdot N_{Ca}^{B_2}$. This model was recently adapted for drainage hysteresis in liquid bridges as follows (Shi et al., 2018): $\frac{\cos\theta_R - \cos\theta_{S,\ DR}}{\cos\theta_{S,\ DR}+1} = B_1 \cdot N_{Ca}^{B_2}$. We applied these models to estimate drainage and imbibition hysteresis (Fig. 12b). Our contact angles were fitted with B_1=18.8 and B_2=1.0 for drainage and B_1=0.29 and B_2=0.16 for imbibition, but the correlation was poor with R^2=0.38 and R^2=0.47, respectively. Note, however, that for field-scale implications drainage/imbibition hysteresis is less important than the dynamic one ($\Delta\theta_D$) as discussed above. The $\Delta\theta_D$ can be used to estimate drainage/imbibition hydrogen-water relative permeability curves.

3.4.3. Discussion on measurement techniques

Literature data on hydrogen contact angles is scare, despite being highly relevant for wettability and relative permeability estimations. Our contact angle measurements matched well with θ_S reported for hydrogen in Berea sandstone (Hashemi et al., 2021) and with θ_R in Vosges sandstone (Yekta et al., 2018), but were higher than θ_E in basaltic (Al-Yaseri and Jha 2021) and θ_D in quartz (Iglauer et al., 2021) rocks. Inconsistency between literature results may be related to different experimental conditions, measurement techniques, and cleaning procedures (Iglauer et al., 2015). Contact angle dependency on pressure and temperature was showed with tilted plate method (Al-Yaseri and Jha 2021; Iglauer et al., 2021) and core-scale steady-state drainage (Yekta et al., 2018), whereas the captive-bubble method did not identify any pressure, temperature and salinity effects (Hashemi et al., 2021). Micromodel-based measurement technique used in this study is unconventional and relatively novel, previously applied by a few CO_2 studies only (Hu et al., 2017; Jafari and Jung 2017; Chang et al., 2020). However, this measurement method is valuable as it provides direct static and dynamic contact angle measurements in micromodel pores, thus representing multiphase flow in porous media more accurately than indirect measurements. Our results can enhance understanding of wettability as well as relative permeability and capillary pressure hysteresis, which are well-recognized in natural gas storage (Colonna et al., 1972) but not appropriately studied for hydrogen.

Despite being valuable for wettability and hysteresis determination in real pore structures, our measurement technique possessed several sources of uncertainties. The first source was related to the identification of the hydrogen-grain contact line, caused by non-planar grain surfaces and shadows due to non-vertical pore walls. To minimize this error, sufficiently long contact lines were selected on nearly flat grains. The second source of uncertainties was linked to the tangent line drawn along the hydrogen-water curvature. The third source was caused by random hydrogen distribution, which did not allow to measure all four contact angle types in the same pore, enhancing local effect on the measurements. To suppress the effect of uncertainties, the contact angles measurements were repeated five times in each measurement and average values were reported together with uncertainties, thus adding reliability to our measurements.

3.5. Discussion on implications and methodologies

Our results have several field scale implications. Hydrogen saturation after drainage increased with increasing injection rate, suggesting the storage site development is the most efficient at high injection rates. Nevertheless, the Roof snap-off was observed at the highest injection rate ($N_{Ca} = 3.84 \cdot 10^{-4}$). This resulted in hydrogen disconnection and trapping, potentially leading to lower storage efficiencies. The observations of the drainage snap-off show that current pore-scale modelling approaches, based on invasion percolation and static snap-off criteria, should be revisited (Roman et al., 2017; Herring et al., 2018). Note that UHS field scale projects will use intermittent hydrogen injections with various frequencies and loads, potentially resulting in reconnection of the residually trapped hydrogen.

If the drainage snap-off occurs at $N_{Ca} = 3.84 \cdot 10^{-4}$, the corresponding field-scale injection rate would be approximately 1.7 million Sm^3/d (standard cubic metre per day), based on the perforation length of 30 m and experimental injection velocity. Lower hydrogen injection rates (< 1.7 million Sm^3/d) may therefore be preferred to avoid the hydrogen disconnection. Note, however, that the laboratory N_{Ca} should be applied for field-scale implications with caution because they do not account for important reservoir parameters such as gravity, heterogeneity, and wettability.

Despite low solubility in water, direct pore-scale hydrogen dissolution was observed in our work. Hydrogen dissolution is undesired in storage projects due to loss of recoverable hydrogen (Carden and Paterson 1979). The observed dissolution emphasizes the importance of the cushion gas composition, where other-than-hydrogen cushion gases with low solubility in water are preferred. Moreover, hydrogen dissolution may be enhanced by water encroachment during withdrawal, as well as the buoyancy-driven hydrogen injection from the reservoir bottom. Non-equilibrium dissolution, if valid at the reservoir-scale, is in turn more favourable compared with the equilibrium one, leading to slower hydrogen dissolution. Under subsurface conditions, hydrogen dissolution kinetics is expected to change according to the literature solubility data: hydrogen solubility increases with increasing pressure and decreases with increasing salinity (Chabab et al., 2020).

The numerical approach dominates the UHS literature, relying on the parameter approximations without exact knowledge. Since the UHS is an emerging field, the models need to be validated with hydrogen laboratory data. Microfluidics offers systematic investigation of the parameter space to collaborate model development. However, upscaling of microfluidic experiments to field scale should be implemented with caution, due to their 2D nature with lack of gravitational effects and heterogeneity. Furthermore, the interactions between viscous/capillary and gravitational forces become more pronounced at field scale. The most suitable way to upscale the microfluidic experiments is through pore-scale modelling. For future work, we recommend coupling microfluidic experiments and pore-scale modelling to support the proposed models of hydrogen behaviour in porous media.

4. Conclusions

Microfluidic drainage and imbibition experiments were performed to examine the hydrogen-water flow in a natural sandstone geometry. In situ live camera monitoring provided qualitative data describing hydrogen displacement and trapping mechanisms. Hydrogen dissolution kinetics and contact angles were quantified using image processing. We summarize our main findings as follows:

- Hydrogen saturation after drainage increased with increasing capillary number (N_{Ca}). Hydrogen phase connectivity was generally high except for high-N_{Ca} ($3.84 \cdot 10^{-4}$) drainage, where disconnected hydrogen phase established due to Roof snap-off.
- Hydrogen displacement during imbibition was mainly governed by I1 imbibition mechanism, whereas hydrogen disconnection with subsequent residual trapping was generally triggered by I2 imbibition mechanism. Hydrogen dissolution occurred at one end of the bubble mainly.
- Hydrogen dissolution kinetics was quantified showing that average depletion rate of individual hydrogen bubbles ranged between $2.3 \cdot 10^{-12}$ to $22 \cdot 10^{-12}$ g/*sec* and appeared to depend on N_{Ca} and initial bubble size. The average global hydrogen depletion rate varied between $3.6 \cdot 10^{-10}$ to $277 \cdot 10^{-10}$ g/*sec*. The average dissolved hydrogen concentration in injected water mass was within the range of $6.4 \cdot 10^{-4}$ to $11 \cdot 10^{-4}$ mol/kg, which was only 16.0–28.3% of the literature solubility, demonstrating the non-equilibrium dissolution.
- Static and dynamic contact angles ranged from 17 to 56°, confirming the non-wetting hydrogen nature. The equilibrium angle calculations fit Class II behaviour. Hysteresis was quantified showing that dynamic contact angle hysteresis was higher than the static.

CRediT authorship contribution statement

Maksim Lysyy: Conceptualization, Methodology, Formal analysis, Investigation, Writing – original draft, Visualization. **Geir Ersland:** Conceptualization, Formal analysis, Writing – review & editing, Supervision, Project administration. **Martin Fernø:** Conceptualization, Formal analysis, Writing – review & editing, Visualization, Supervision, Project administration.

Declaration of Competing Interest

None.

Acknowledgements

The authors would like to thank the Department of Physics and Technology, the University of Bergen for financial support.

Supplementary materials

Supplementary material associated with this article can be found, in the online version, at doi:10.1016/j.advwatres.2022.104167.

References

Akbarabadi, M., Piri, M., 2013. Relative permeability hysteresis and capillary trapping characteristics of supercritical CO2/brine systems: an experimental study at reservoir conditions. Adv. Water Resour. 52, 190–206.
Al-Yaseri, A., Jha, N.K., 2021. On hydrogen wettability of basaltic rock. J. Pet. Sci. Eng. 200.
al, N.S.M.e, 2022. A review on underground hydrogen storage: insight into geological sites, influencing factors and future outlook. Energy Reports.
Alcorn, Z.P., Foyen, T., Gauteplass, J., Benali, B., Soyke, A., Ferno, M., 2020. Pore- and core-scale insights of nanoparticle-stabilized foam for co2-enhanced oil recovery. Nanomaterials 10 (10).
Andrew, M., Menke, H., Blunt, M.J., Bijeljic, B., 2015. The imaging of dynamic multiphase fluid flow using synchrotron-based x-ray microtomography at reservoir conditions. Transp. Porous Media 110 (1), 1–24.
Armstrong, R.T., Berg, S., 2013. Interfacial velocities and capillary pressure gradients during Haines jumps. Phys. Rev. E 88 (4).
Beckingham, L.E., Winningham, L., 2020. Critical knowledge gaps for understanding water-rock-working phase interactions for compressed energy storage in porous formations. ACS Sustain. Chem. Eng. 8 (1), 2–11.
Berta, M., Dethlefsen, F., Ebert, M., Schafer, D., Dahmke, A., 2018. Geochemical effects of millimolar hydrogen concentrations in groundwater: an experimental study in the context of subsurface hydrogen storage. Environ. Sci. Technol. 52 (8), 4937–4949.
Bo, Z., Zeng, L., Chen, Y., Xie, Q., 2021. Geochemical reactions-induced hydrogen loss during underground hydrogen storage in sandstone reservoirs. Int. J. Hydrogen Energy.
Buchgraber, M., Al-Dossary, M., Ross, C.M., Kovscek, A.R., 2012a. Creation of a dual-porosity micromodel for pore-level visualization of multiphase flow. J. Pet. Sci. Eng. 86-87, 27–38.
Buchgraber, M., Kovscek, A.R., Castanier, L.M., 2012b. A study of microscale gas trapping using etched silicon micromodels. Transp. Porous Media 95 (3), 647–668.
Cao, S.C., Dai, S., Jung, J., 2016. Supercritical CO2 and brine displacement in geological carbon sequestration: micromodel and pore network simulation studies. Int. J. Greenhouse Gas Control 44, 104–114.
Carden, P.O., Paterson, L., 1979. Physical, chemical and energy aspects of underground hydrogen storage. Int. J. Hydrogen Energy 4 (6), 559–569.
Chabab, S., Theveneau, P., Coquelet, C., Corvisier, J., Paricaud, P., 2020. Measurements and predictive models of high- pressure H-2 solubility in brine (H2O+NaCl) for underground hydrogen storage application. Int. J. Hydrogen Energy 45 (56), 32206–32220.
Chang, C., Kneafsey, T.J., Wan, J.M., Tokunaga, T.K., Nakagawa, S., 2020. Impacts of mixed-wettability on brine drainage and supercritical CO2 storage efficiency in a 2.5-D heterogeneous micromodel. Water Resour. Res. 56 (7).
Chang, C., Zhou, Q.L., Kneafsey, T.J., Oostrom, M., Ju, Y., 2019. Coupled supercritical CO2 dissolution and water flow in pore-scale micromodels. Adv. Water Resour. 123, 54–69.
Chang, C., Zhou, Q.L., Kneafsey, T.J., Oostrom, M., Wietsma, T.W., Yu, Q.C., 2016. Pore-scale supercritical CO2 dissolution and mass transfer under imbibition conditions. Adv. Water Resour. 92, 142–158.
Chang, C., Zhou, Q.L., Xia, L., Li, X.Y., Yu, Q.C., 2013. Dynamic displacement and non-equilibrium dissolution of supercritical CO2 in low-permeability sandstone: an experimental study. Int. J. Greenhouse Gas Control 14, 1–14.
Chatzis, I., Morrow, N.R., Lim, H.T., 1983. Magnitude and detailed structure of residual oil saturation. Soc. Pet. Eng. J. 23 (2), 311–326.
Chen, L., Wang, M.Y., Kang, Q.J., Tao, W.Q., 2018. Pore scale study of multiphase multicomponent reactive transport during CO2 dissolution trapping. Adv Water Resour 116, 208–218.
Colonna, J., Brissaud, F., Millet, J.L., 1972. Evolution of capillarity and relative permeability hysteresis. Soc. Pet. Eng. J. 12 (1), 28-&.
De Lucia, M., Pilz, P., Liebscher, A., Kühn, M., 2015. Measurements of H2 solubility in saline solutions under reservoir conditions: preliminary results from project H2STORE. Energy Procedia 76, 487–494.
Deng, W., Balhoff, M., Cardenas, M.B., 2015. Influence of dynamic factors on nonwetting fluid snap-off in pores. Water Resour. Res. 51 (11), 9182–9189.
Duchateau, C., Broseta, D., 2012. A simple method for determining brine-gas interfacial tensions. Adv. Water Resour. 42, 30–36.
Eral, H.B., 't Mannetje, D.J.C.M., Oh, J.M., 2013. Contact angle hysteresis: a review of fundamentals and applications. Colloid. Polym. Sci. 291 (2), 247–260.
Flesch, S., Pudlo, D., Albrecht, D., Jacob, A., Enzmann, F., 2018. Hydrogen underground storage-Petrographic and petrophysical variations in reservoir sandstones from laboratory experiments under simulated reservoir conditions. Int. J. Hydrogen Energy 43 (45), 20822–20835.
Friedman, S.P., 1999. Dynamic contact angle explanation of flow rate-dependent saturation-pressure relationships during transient liquid flow in unsaturated porous media. J. Adhes. Sci. Technol. 13 (12), 1495–1518.
Hashemi, L., Blunt, M., Hajibeygi, H., 2021a. Pore-scale modelling and sensitivity analyses of hydrogen-brine multiphase flow in geological porous media. Sci. Rep. 11 (1).
Hashemi, L., Glerum, W., Farajzadeh, R., Hajibeygi, H., 2021b. Contact angle measurement for hydrogen/brine/sandstone system using captive-bubble method relevant for underground hydrogen storage. Adv. Water Resour. 154.
Herring, A.L., Gilby, F.J., Li, Z., McClure, J.E., Turner, M., Veldkamp, J.P., Beeching, L., Sheppard, A.P., 2018. Observations of nonwetting phase snap-offduring drainage. Adv. Water Resour. 121, 32–43.
Hoffman, R.L., 1983. A study of the advancing interface .2. Theoretical prediction of the dynamic contact-angle in liquid gas systems. J. Colloid Interface Sci. 94 (2), 470–486.
Hornbrook, J.W., Castanier, L.M., Pettit, P.A., 1991. Observation of foam/oil interactions in a new, high-resolution micromodel. In: SPE Annual Technical Conference and Exhibition. Dallas, Texas, Society of Petroleum Engineers.
Hu, R., Wan, J.M., Kim, Y., Tokunaga, T.K., 2017. Wettability impact on supercritical CO2 capillary trapping: pore-scale visualization and quantification. Water Resour. Res. 53 (8), 6377–6394.
Iglauer, S., Ali, M., Keshavarz, A., 2021. Hydrogen wettability of sandstone reservoirs: implications for hydrogen geo-storage. Geophys. Res. Lett. 48 (3).
Iglauer, S., Pentland, C.H., Busch, A., 2015. CO2 wettability of seal and reservoir rocks and the implications for carbon geo-sequestration. Water Resour. Res. 51 (1), 729–774.
Jafari, M., Jung, J., 2017. Direct measurement of static and dynamic contact angles using a random micromodel considering geological CO2 sequestration. Sustainability 9 (12).
Jafari, M., Jung, J., 2019. Salinity effect on micro-scale contact angles using a 2D micromodel for geological carbon dioxide sequestration. J. Pet. Sci. Eng. 178, 152–161.
Jiang, T.S., Oh, S.G., Slattery, J.C., 1979. Correlation for dynamic contact-angle. J. Colloid Interface Sci. 69 (1), 74–77.
Joanny, J.F., Degennes, P.G., 1984. A model for contact-angle hysteresis. J. Chem. Phys. 81 (1), 552–562.
Johnson, R.E., Dettre, R.H., 1964. Contact angle hysteresis .3. Study of an idealized heterogeneous surface. J. Phys. Chem. 68 (7), 1744-&.
Kuchin, I.V., Starov, V.M., 2016. Hysteresis of the contact angle of a meniscus inside a capillary with smooth, homogeneous solid walls. LangmuirLangmuir 32 (21), 5333–5340.
Lenormand, R., Touboul, E., Zarcone, C., 1988. Numerical-models and experiments on immiscible displacements in porous-media. J. Fluid Mech. 189, 165–187.
Lenormand, R., Zarcone, C., Sarr, A., 1983. Mechanisms of the displacement of one fluid by another in a network of capillary ducts. J. Fluid Mech. 135 (Oct), 337–353.
Li, D.D., Beyer, C., Bauer, S., 2018. A unified phase equilibrium model for hydrogen solubility and solution density. Int. J. Hydrogen Energy 43 (1), 512–529.
Li, X.X., Fan, X.F., Askounis, A., Wu, K.J., Sefiane, K., Koutsos, V., 2013. An experimental study on dynamic pore wettability. Chem. Eng. Sci. 104, 988–997.
Lopez-Lazaro, C., Bachand, P., Moretti, I., Ferrando, N., 2019. Predicting the phase behavior of hydrogen in NaCl brines by molecular simulation for geological applications. Bsgf-Earth Sci. Bull. 190.
Lord, A.S., Kobos, P.H., Borns, D.J., 2014. Geologic storage of hydrogen: scaling up to meet city transportation demands. Int. J. Hydrogen Energy 39 (28), 15570–15582.
Lubon, K., Tarkowski, R., 2021. Influence of capillary threshold pressure and injection well location on the dynamic CO2 and H-2 storage capacity for the deep geological structure. Int. J. Hydrogen Energy 46 (58), 30048–30060.
Lysyy, M., Ferno, M., Ersland, G., 2021. Seasonal hydrogen storage in a depleted oil and gas field. Int. J. Hydrogen Energy 46 (49), 25160–25174.
Kanaani, Mahdi, S, B., Asadian-Pakfar, Mojtaba, 2022. Role of cushion gas on underground hydrogen storage in depleted oil reservoirs. J. Energy Storage.
Massoudi, R., King, A.D., 1974. Effect of pressure on surface-tension of water - adsorption of low-molecular weight gases on water at 25 degrees. J. Phys. Chem. 78 (22), 2262–2266.
Moebius, F., Or, D., 2012. Interfacial jumps and pressure bursts during fluid displacement in interacting irregular capillaries. J. Colloid Interface Sci. 377, 406–415.

Mohanty, K.K., Davis, H.T., Scriven, L.E., 1987. Physics of oil entrapment in water-wet rock. SPE Reservoir Eng. 2 (01), 113–128.
Morrow, N.R., 1975. Effects of surface-roughness on contact angle with special reference to petroleum recovery. J. Can. Pet. Technol. 14 (4), 42–53.
Ozarslan, A., 2012. Large-scale hydrogen energy storage in salt caverns. Int. J. Hydrogen Energy 37 (19), 14265–14277.
Panfilov, M., 2010. Underground storage of hydrogen: in situ self-organisation and methane generation. Transp. Porous Media 85 (3), 841–865.
Panfilov, M., 2016. Underground and pipeline hydrogen storage. Compendium of Hydrogen Energy. Woodhead Publishing.
Paterson, L., 1983. The implications of fingering in underground hydrogen storage. Int. J. Hydrogen Energy 8 (1), 53–59.
Pérez, A., Pérez, E., Dupraz, S., Bolcich, J., 2016. In: Patagonia Wind - Hydrogen Project: Underground Storage and Methanation. *21st world hydrogen energy conference*. Zaragoza, Spain.
Pruess, K., Spycher, N., 2007. ECO2N - a fluid property module for the TOUGH2 code for studies of CO2 storage in saline aquifers. Energy Convers. Manage. 48 (6), 1761–1767.
Roman, S., Abu-Al-Saud, M.O., Tokunaga, T., Wan, J.M., Kovscek, A.R., Tchelepi, H.A., 2017. Measurements and simulation of liquid films during drainage displacements and snap-off in constricted capillary tubes. J. Colloid Interface Sci. 507, 279–289.
Roof, J.G., 1970. Snap-off of oil droplets in water-wet pores. Soc. Pet. Eng. J. 10 (1), 85-&.
Seebergh, J.E., Berg, J.C., 1992. Dynamic wetting in the low capillary number regime. Chem. Eng. Sci. 47 (17–18), 4455–4464.
Shi, Z., Zhang, Y., Liu, M.C., Hanaor, D.A.H., Gan, Y.X., 2018. Dynamic contact angle hysteresis in liquid bridges. Colloids Surfaces a-Physicochem. Eng. Aspects 555, 365–371.
Smigan, P., Greksak, M., Kozankova, J., Buzek, F., Onderka, V., Wolf, I., 1990. Methanogenic bacteria as a key factor involved in changes of town gas stored in an underground reservoir. FEMS Microbiol. Ecol. 73 (3), 221–224.
Tadmor, R., 2004. Line energy and the relation between advancing, receding, and young contact angles. LangmuirLangmuir 20 (18), 7659–7664.
Valvatne, P.H., Blunt, M.J., 2004. Predictive pore-scale modeling of two-phase flow in mixed wet media. Water Resour. Res. 40 (7).
Wu, D.S., Hu, R., Lan, T., Chen, Y.F., 2021. Role of pore-scale disorder in fluid displacement: experiments and theoretical model. Water Resour. Res. 57 (1).
Yekta, A.E., Manceau, J.C., Gaboreau, S., Pichavant, M., Audigane, P., 2018. Determination of hydrogen-water relative permeability and capillary pressure in sandstone: application to underground hydrogen injection in sedimentary formations. Transp. Porous Media 122 (2), 333–356.
Zhang, C.Y., Oostrom, M., Wietsma, T.W., Grate, J.W., Warner, M.G., 2011. Influence of viscous and capillary forces on immiscible fluid displacement: pore-scale experimental study in a water-wet micromodel demonstrating viscous and capillary fingering. Energy Fuels 25 (8), 3493–3505.